INTERNATIONAL ATOMIC ENERGY AGENCY

CONF-940933--48

FIFTEENTH INTERNATIONAL CONFERENCE ON PLASMA PHYSICS AND CONTROLLED NUCLEAR FUSION RESEARCH

Seville, Spain, 26 September – 1 October 1994

IAEA-CN-60/A3/5-P-13

Predictions of Fast Wave Heating, Current Drive, and Current Drive Antenna Arrays for Advanced Tokamaks

D. B. Batchelor, F. W. Baity, M. D. Carter, R. H. Goulding, G. R. Hanson, D. J. Hoffman, G. R. Haste, E. F. Jaeger, M. Murakami, D. A. Rasmussen, P. M. Ryan, D. W. Swain, D. C. Stallings, J. B. Wilgen, and C. Y Wang
Oak Ridge National Laboratory
P. O. Box 2009
Oak Ridge, TN 37831-8071

P. T. Bonoli and M. Porkolab
Massachusetts Institute of Technology
167 Albany Street
Cambridge, MA 02139

R. Majeski, J. H. Rogers, G. Schilling, J. E. Schilling, J. E. Stevens, and R. Wilson
Princeton Plasma Physics Laboratory
P. O. Box 451
Princeton, NJ 08543

P. Moroz, M. H. Bettenhausen, and J. E. Scharer
University of Wisconsin
1500 Johnson Drive
Madison, WI 53706-1687

Y. L. Ho
SAIC
10260 Camus Point Drive, MS-32
San Diego, CA 92121

IAEA-CN-60/A3/5-P-13

Predictions of Fast Wave Heating, Current Drive, and Current Drive Antenna Arrays for Advanced Tokamaks

Abstract: The objective of the advanced tokamak program is to optimize plasma performance leading to a compact tokamak reactor through active, steady state control of the current profile using non-inductive current drive and profile control. To achieve these objectives requires compatibility and flexibility in the use of available heating and current drive systems - ion cyclotron radio frequency (ICRF), neutral beams, and lower hybrid. For any advanced tokamak, the following are important challenges to effective use of fast waves in various roles of direct electron heating, minority ion heating, and current drive:

1. To employ the heating and current drive systems to give self-consistent pressure and current profiles leading to the desired advanced tokamak operating modes.

2. To minimize absorption of the fast waves by parasitic resonances, which limit current drive.

3. To optimize and control the spectrum of fast waves launched by the antenna array for the required mix of simultaneous heating and current drive.

We have addressed these issues using theoretical and computational tools developed at a number of institutions by benchmarking the computations against available experimental data and applying them to the specific case of TPX.

1. Self-consistent advanced tokamak heating and current drive scenarios

A large number of operating scenarios have been identified for TPX. These are conveniently grouped into three categories: 1) standard high-beta tokamak with operations near limits in β and q_ψ identified by the present tokamak data base, 2) high bootstrap/first stable tokamak with operation at bootstrap fraction exceeding 66% such as identified in the ARIES-I reactor study, 3) and advanced performance tokamak based on the assumption that confinement improvement factors significantly exceeding H-mode factor = 2 and beta significantly exceeding $\beta_n = 3.5$ can be achieved by proper shaping and profile control. We have used the ACCOME code [1] to demonstrate that for each of these categories, equilibria can be produced having self-consistent pressure and current profiles including fast wave, neutral beam, lower hybrid, and bootstrap currents. The transport and stability of these equilibria is still under investigation.

For standard tokamak operation at $B_0 = 4$ T, assuming an H-mode or VH-mode confinement improvement factor of H = 3, scenarios are found having $T_e(0) = T_D(0)$ up to 15 keV and $n_e(0) = 1.0 \times 10^{20}$ m^{-3}, $I_P = 1.74$ MA, $q_{95} = 3.4$, and $\beta_N = 1.94$. Of the 1.7 MA of plasma current, 860 kA is fast wave driven current, 280 kA is from beam injection, 73 kA is from lower hybrid, and 490 kA is bootstrap. In modeling with the PICES 2-D full wave code, we confirm that in this scenario currents over 800 kA can be driven by the available 8 MW of fast wave power. Because of the highly peaked FW current profile, $q_0 << 1$ if sawtooth or other current profile broadening processes are neglected. The actual consequence of the highly peaked fast wave current drive (FWCD) profile is an important matter for further investigation.

Numerous high bootstrap scenarios have been developed with bootstrap fractions in the range $0.6 < f_{BS} < 0.9$. In these cases the neutral beams provide ample seed

current, although full beam and ICRF power are required for plasma heating. An example of a 70% bootstrap fraction scenario is shown in Fig. 1(a). Here $T_e(0) = T_D(0) = 15$ keV and $n_e(0) = 1.0 \times 10^{20}$ m^{-3} with $I_P = 1.77$ MA, $B_0 = 3$ T, $q_0 = 1.3$, $q_{95} = 4.3$, and $\beta_N = 3.58$. The driven current consists of 400 kA from neutral injection, 90 kA from lower hybrid, and 63 kA of on-axis fast wave current drive.

Among the advanced performance scenarios investigated, some of the most promising are those that seek to obtain improved confinement using reversed shear, which is thought to explain the PEP modes on JET. Assuming an H-mode factor of 2.7, we obtain scenarios having T(0) up to 20 keV and f_{BS} up to 0.92 at I_P of 2.04 MA. A typical example is shown in Fig. 1(b). where, in this case, fast waves are used to drive a countercurrent of $I_{FW} = -136$ kA to maintain $q_0 > 2$. In this scenario $T_e(0) = T_D(0) = 14$ keV and $n_e(0) = 0.9 \times 10^{20}$ m^{-3} with $I_P = 1.63$ MA, $q_{min} = 1.8$, $q_{95} = 3.4$, and $\beta_N = 4.3$. The bootstrap fraction is 75%, whereas $I_{NB} = 425$ kA and $I_{LH} = 126$ kA. To control the shear reversal point, it is necessary to operate in an n_e, T_e, B_T regime, which keeps the lower hybrid deposition layer at $0.7 < \rho < 0.9$ and which maximizes I_{LH}.

2. Fast wave current drive physics

TPX, with its comparatively large aspect ratio, is a very attractive machine for fast wave current drive. There is a frequency window between about 45 and 48 MHz for which there are no parasitic ion resonances and a higher frequency window between about 78 and 80 MHz for which the Ω_H resonance is out of the machine on the high field side and the $3\Omega_D$ resonance, although present, is near enough to the edge that parasitic absorption can be acceptable. We have investigated the current drive efficiency, the effect of parasitic resonances, and the controllability of the driven current profile using the 2-D full wave RF codes PICES, FISIC, and FASTWA [1]. These codes are in reasonable agreement with the limited fast wave current drive data base from DIII-D and with the fast wave direct electron heating experiments on TFTR. We find in TPX that at $T_e(0) = 10$ keV, the current drive efficiency is typically $\gamma \sim 0.1 \times 10^{20}$ A/w/m^2, so that, for example, at $n_e(0) = 1 \times 10^{20}$ m^{-3} the fast wave driven current is ~600 kA. In the 45 MHz frequency range, parasitic absorption is not significant even though electron absorption is weak. However, current drive efficiency is limited by upshift of $k_{||}$ due to the poloidal field. Electron absorption is much stronger at the higher frequency, however, up to ~35% of the power can be absorbed by third harmonic D depending on the distribution of beam injected D ions. Despite the parasitic ion absorption, the total current drive efficiency is slightly higher at the higher frequency.

3. Analysis and design of fast wave current drive antenna arrays

The performance of ICRF antenna arrays, both with regard to the launched power spectrum and their interaction with edge plasma, is sensitively dependent on details of the self-consistent currents in the antenna structure and in the plasma. Recently, there has been a considerable advance in our understanding of the physics of these launching structures through the development of 3-D modeling codes. RF antenna arrays are inherently 3-D structures. The antenna source currents and many of the induced image currents cannot be adequately modeled in 2-D. Also, the plasma response is inherently 3-D since the coupling properties of the plasma depend sensitively on the poloidal mode spectrum.

The RANT3D code [2] and the WICS code [3] both employ Fourier expansions in the toroidal and poloidal directions which simplify the 3-D geometry somewhat by neglecting the detailed structure of the Faraday shield, but which are well suited to calculating the performance of large arrays of antennas. The plasma response is

included by solving the 1-D radial wave equation assuming uniformity in the toroidal and poloidal directions and matching boundary conditions at the plasma vacuum interface. At present the strap current distribution is specified using information from bench measurements and 3-D magnetostatic codes. The WICS code also models an idealized Faraday shield by imposing an appropriate boundary condition. The RANT3D code has great flexibility in that multiple recesses are allowed, and recesses can be placed within recesses so that antennas with septa of varying height, antennas that protrude beyond the tokamak wall, and antennas with limiters can be modeled. Figure 2(a) shows the geometry of recesses and current straps used in the RANT3D modeling of the Bay M antenna on TFTR. Recesses 3 through 6 model openings in the tokamak first wall. We have also used the ARGUS code [4], which employs finite difference methods in the vacuum region to treat the local 3-D structure in minute detail (including discrete Faraday shield). Coupling to the plasma is achieved using an iterative scheme by which the vacuum solution in real space (y,z) is Fourier transformed and matched to the 1-D (k_y,k_z)-space solutions in the plasma. In this code the antenna is excited by specifying the voltage across a gap in the back-plane. Figure 2(b) shows the geometry, including Faraday shield bars, of one-fourth of the TFTR Bay-M mockup antenna. The computational domain has been reduced to one-fourth by appealing to symmetry.

To demonstrate the accuracy of these codes, we concentrate on comparison of calculated versus experimental measurements of loading, a fundamental quantity of antenna performance. This is made possible using high resolution edge-plasma density profiles obtained using a two-frequency, differential-phase reflectometer system installed in the Bay M ICRF antenna on TFTR [5]. To make quantitative comparisons, we have also employed 1) a circuit model for the antenna and transmission system that allows current, voltage, and power measurements made remote from the antenna box to be converted to the experimental radiation resistance at the current strap, and 2) a 3-D magnetostatic model to determine the phase velocity of the current wave on the strap and to determine the Faraday shield transmission coefficient [6]. In the experiments studied, the antenna-to-plasma gap was varied by changing the major radius of the plasma. The full plasma density profiles for this series of shots were obtained by combining the reflectometer edge profile with the multi-channel interferometer central density profile. An example of two of the profiles of this series is shown in Fig. 3(a). The profiles are peaked in the center, have a steep density gradient near the edge (presumably the result of scrape-off on the inner bumper limiter), and have an exponential decay to the edge. Figures 3(b) and 3(c) compare experimental values with calculations using the RANT3D and RANT2D codes. We can see that the agreement between experiment and the 3-D calculations is extremely good whereas the 2-D model overestimates loading by quite a large amount at small gap spacing. We have studied the sensitivity of the results to a number of factors. We find that to achieve good agreement with the experiment it is necessary to include: 1) the fact that the antenna protrudes form the vessel wall [as represented by recesses 3 through 6 of Fig. 2(a)], 2) the strong poloidal dependance of the plasma surface impedance, and 3) the tendency of the source current to concentrate toroidally on the edges of the current strap.

We find that 3-D effects can also have a significant effect on launched wave spectrum, particularly for phase shifts less than 180° and for arrays with few elements. The TPX 12 strap antenna produces a very efficient spectrum for current drive, mainly due to the array factor for the 12-element array. The main lobe is sufficiently narrow that the wave spectrum can be well matched to the thermal electrons, while the countercurrent side lobe is so slow that little power is coupled and very little current is driven. However, the image currents in the sidewalls and septa reduce the coupling at small $k_{||}$ relative to the predictions of 2-D models. Depending on details of the edge density profile, this can result in a decrease in total loading of ~30%.

Acknowledgements:

This research was sponsored by the Office of Fusion Energy, U.S. Department of Energy, under contract DE-AC05-84OR21400 with Martin Marietta Energy Systems, Inc.

References:

[1] BONOLI, P.T., Radio Frequency Power in Plasmas 10th Topical Conference, AIP Conf. Proc. 289 (1994) 192.

[2] CARTER, M.D., et al., to be published (1994).

[3] BETTENHAUSEN, M.H., and SCHARER, J.E., Radio Frequency Power in Plasmas 10th Topical Conference, AIP Conf. Proc. 289 (1994) 363.

[4] HO, Y.L., et al., Radio Frequency Power in Plasmas 10th Topical Conference, AIP Conf. Proc. 289 (1994) 359.

[5] HANSON, G.R., et al., Microwave Reflectometry for Edge Density Profile Measurements on TFTR, to be published Plasma Physics and Controlled Fusion.

[6] RYAN, P.M., et al., Fusion Engineering and Design **24** (1994) 135, and PARK, H. K., Plasma Physics and Controlled Fusion **31** (1989) 2035.

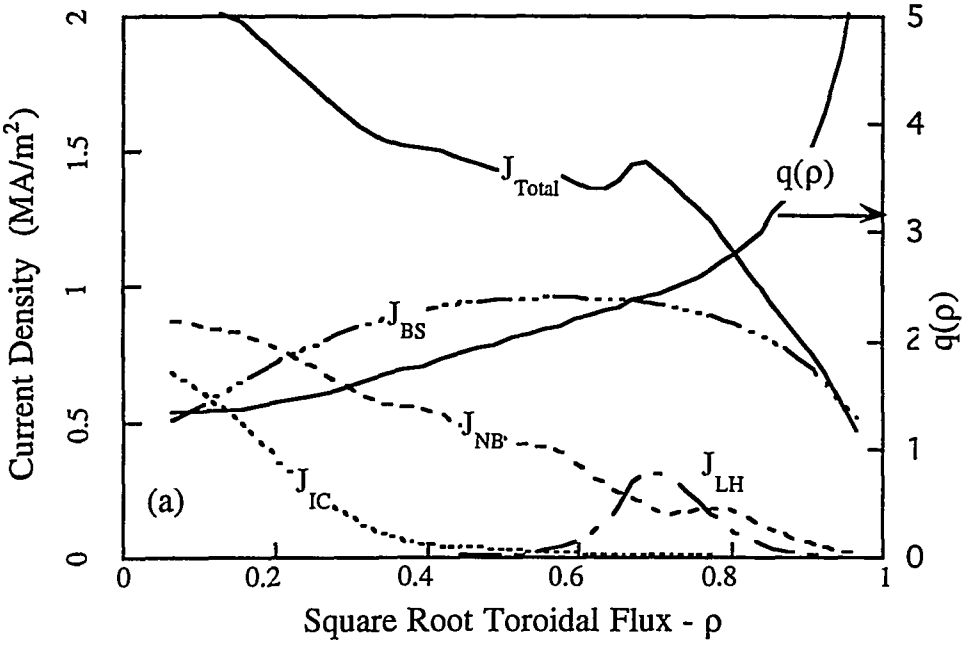

Fig. 1(a) Current density and q profiles for ARIES-I like high bootstrap scenario.

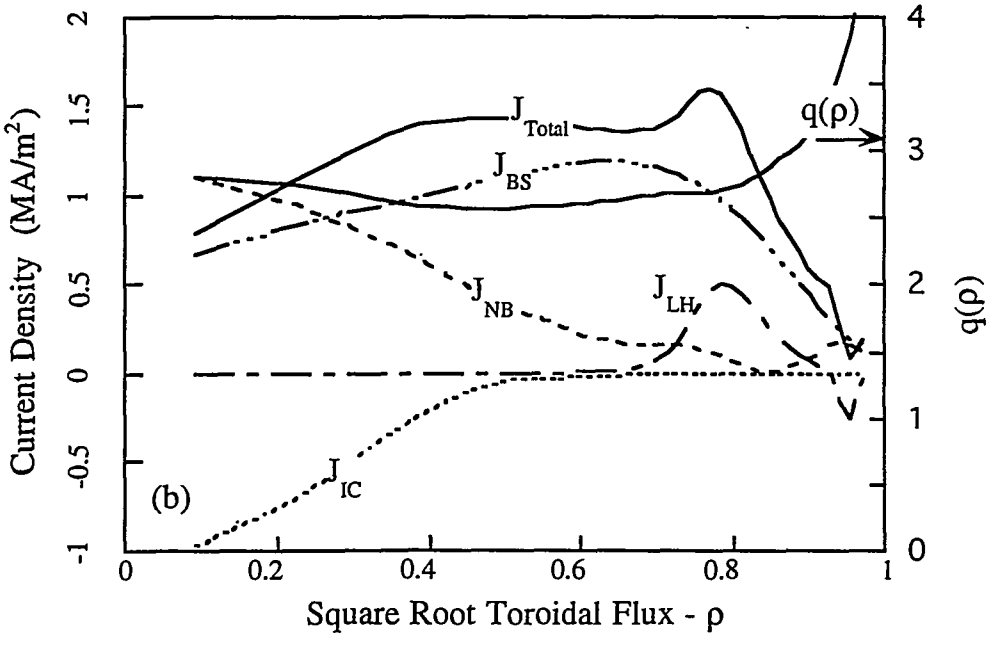

Fig.1(b) Current density and q profiles for Advanced tokamak, reverse shear scenario.

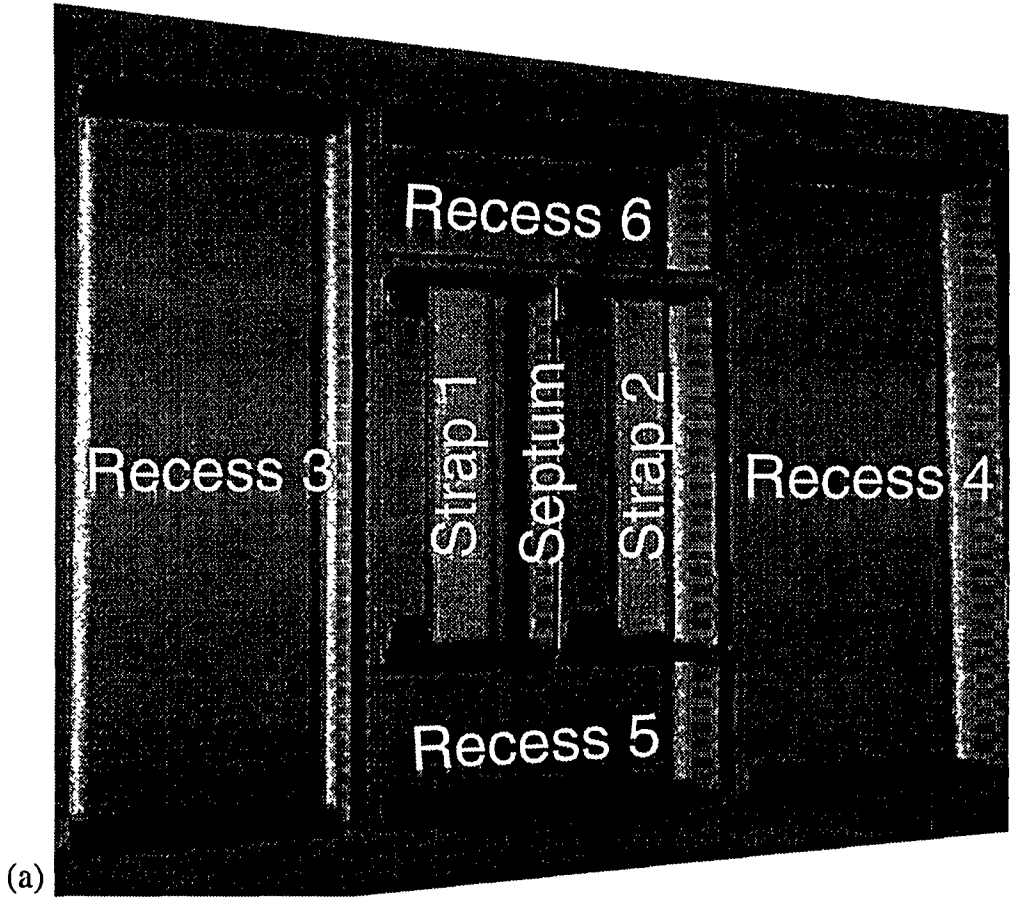

(a)

Fig. 2(a) Geometry of TFTR Bay-M antenna and first wall as used in RANT3D.

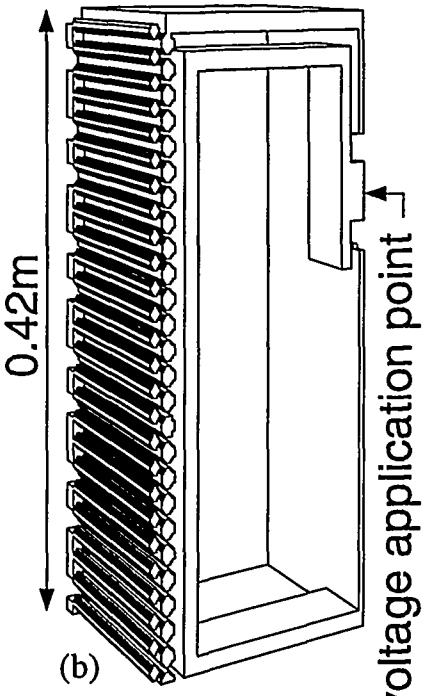

(b)
(Enlarged View)

Fig. 2(b) Geometry of 1/4 of TFTR Bay M mockup used in ARGUS.

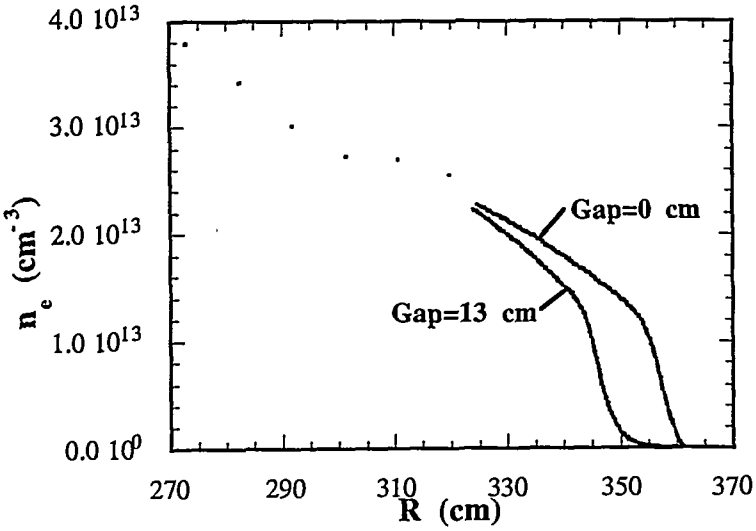

Fig. 3(a) Density profiles for TFTR shots #73701 and 73703 having different gap between plasma edge and antenna.

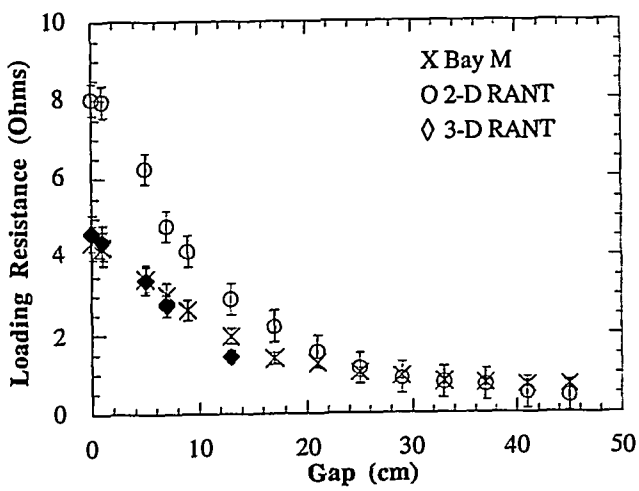

Fig. 3(b) Loading versus gap for monopole phasing.

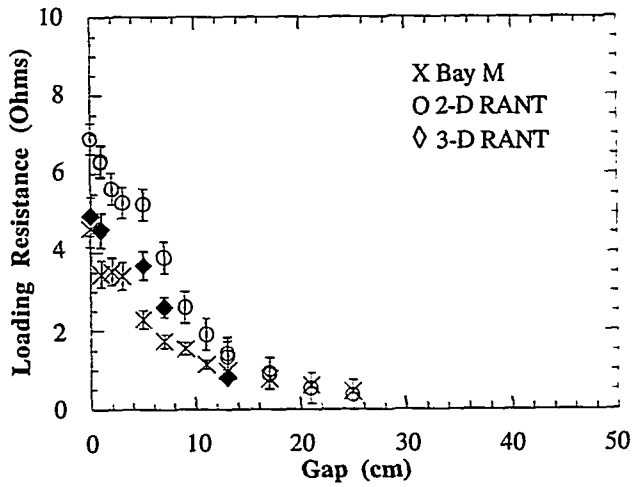

Fig. 3(b) Loading versus gap for dipole phasing.